Journal of Alloys and Compounds 768 (2018) 377–386

Contents lists available at ScienceDirect

Journal of Alloys and Compounds

journal homepage: http://www.elsevier.com/locate/jalcom

Spectroscopic study of phase transitions in ferroelectric $Bi_{0.5}Na_{0.5}Ti_{1-x}Mn_xO_{3-\delta}$ films with enhanced ferroelectricity and energy storage ability

Weili Xu [a], Xin Li [a], Qianqian Li [a], Qinglin Deng [a], Jin-Zhong Zhang [a, *], Kai Jiang [a, **], Yawei Li [a], Liyan Shang [a], Zhigao Hu [a, b], Junhao Chu [a]

[a] Key Laboratory of Polar Materials and Devices (MOE) and Technical Center for Multifunctional Magneto-Optical Spectroscopy (Shanghai), Department of Electronic Engineering, East China Normal University, Shanghai, 200241, China
[b] Collaborative Innovation Center of Extreme Optics, Shanxi University, Taiyuan, Shanxi, 030006, China

ARTICLE INFO

Article history:
Received 27 April 2018
Received in revised form
16 July 2018
Accepted 18 July 2018
Available online 25 July 2018

Keywords:
Lead-free ferroelectrics
Condensed matter spectroscopy
Phase transitions
Enhanced ferroelectric
Energy storage ability

ABSTRACT

Lead-free ferroelectric $Bi_{0.5}Na_{0.5}TiO_3$ (BNT) has attracted considerable attention taking into account environment issues and applications in micro electro mechanical systems. The effects of manganese (Mn) substitution on microstructure, lattice dynamics, and optical properties of BNT films have been investigated by X-ray diffraction, Raman scattering and ellipsometric spectra. The phase transitions as a function of temperature have been systemically explored by temperature-dependent Raman and ellipsometric spectra. The anomalous temperature-dependent behavior of Raman-active modes suggests that there is an intermediate phase between ferroelectric rhombohedral and paraelectric tetragonal phase, which is confirmed by the temperature-dependent optical band gap (E_g) and extinction coefficient (κ) extracted from ellipsometric spectra analysis. And then, a phase diagram as a function of Mn composition has been proposed. Finally, we demonstrate that Mn-dopant is an effective approach to enhance ferroelectric properties, improve energy storage ability, and increase permittivity as well as suppress leakage current. Electrical dielectric responses indicate that there is a critical frequency and polarization relaxation behavior in the films. The present results will be helpful for the application of BNT-based lead-free multifunctional devices.

1. Introduction

$PbZr_{1-x}Ti_xO_3$ (PZT), $Pb(Mg_{1/3}Nb_{2/3})O_3$-$PbTiO_3$ (PMN-PT) and other lead-based ferroelectrics show morphotropic phase boundaries (MPB) system between different competing phases, endowing it with superior piezoelectric response due to symmetry-allowed polarization rotation, which makes it possible to contribute to a wide range of applications such as medical ultrasound, transducer and energy harvesting [1–6]. However, taking into account both environment and health issues, these ferroelectrics are not the best candidates because of containing a large amount of toxic lead. Therefore, finding an environment-friendly lead-free ferroelectric material with performances that can compare favourably with that of the lead-based system becomes a matter of urgency. Note that Bi^{3+} and Pb^{2+} ions share similar electron configuration, ionic radius, number of electrons and a lone electron pair, which contribute to structure distortion and piezoelectric response [7,8]. Bismuth sodium titanate ($Bi_{0.5}Na_{0.5}TiO_3$, abbreviated as BNT) and BNT-based compounds have attracted considerable attention as one of the most promising candidates to replace the widely used lead-based ferroelectrics due to the high Curie temperature ($T_C \sim$ 600 K), excellent remanent polarization ($P_r \sim 38\ \mu C/cm^2$), remarkable relative dielectric constant of approximately 500 at 1 kHz and superior piezoelectric coefficient ($d_{33} \sim 80$ pC/N) [5]. Pure BNT with the distorted perovskite structure ABO_3, where the A-site is simultaneously occupied by Bi and Na cations [8–10]. BNT undergoes a sequence of phase transitions from a cubic structure ($Pm\bar{3}m$) at the temperature above 813 K, to a tetragonal one ($P4bm$) in the range of 783∼813 K, and then to a rhombohedral phase ($R3c$)

* Corresponding author.
** Corresponding author.
E-mail addresses: jzzhang@ee.ecnu.edu.cn (J.-Z. Zhang), kjiang@ee.ecnu.edu.cn (K. Jiang).

https://doi.org/10.1016/j.jallcom.2018.07.213
0925-8388/

at the temperature below 517 K on cooling [8,11]. However, Rao et al. first demonstrated that a pure ferroelectric compound (BNT) exhibits the coexistence of two ferroelectric phases rhombohedral (*R*3*c*) and monoclinic (*Cc*) in its equilibrium state at room temperature [12]. Moreover, a diffuse phase transition region between rhombohedral and tetragonal phases still remains controversial.

The potential applications of thin films for sensors and actuators in micro electro mechanical systems (MEMS) trigger a growing interest in film devices [13]. Whereas, the practical applications of BNT films are seriously limitated due to complicated crystal structure, high leakage current density and dielectric loss [7,14,15]. Therefore, it is urgent to optimize composition and microstructure of BNT-based films to suppress leakage current. Previous researches have verified that alkali ions and oxygen vacancies play a significant role in high leakage current [16–18]. It has been found that Mn element, which is introduced into $BiFeO_3$ [19], KNN [20], $BaTiO_3$ [21] and BNT [22–24] systems, would lead to an enhanced insulating properties [25]. In particular, Mn basically plays a part of an acceptor dopant replacing Ti^{4+}, Nb^{5+} or Fe^{3+} ions in the perovskite structure, which probably exert a tremendous influence on leakage current [18–24]. In addition, few studies have focused on optical properties such as phonon modes, optical constants, band gap and electronic band structure, which deeply imposes restrictions on the future applications of optoelectronic devices [8,11,26,27]. Zhu et al. argued that NBT crystal is of a two-phase mixture with rhombohedral and monoclinic structures at room temperature according to the infrared- and Raman-active modes [8]. Moreover, Zeng et al. obtained a direct band gap of 2.1 eV by using a full potential linearized augmented plane-wave method within a generalized gradient approximation, while it is estimated to be 3.03 eV based on the fit of optical absorption spectrum [11]. Based on the above consideration, phase transitions, optical and electrical properties of pure and element-doped BNT are neither clear nor systematic, which needs a further study in detail.

In this work, the temperature-dependent Raman-active phonon modes and optical band gap are applied to analyze the phase transition of Mn-doped BNT (BNTM) films. The improvement of ferroelectric responses, energy storage ability, leakage current and dielectric properties of BNTM films were investigated in detail. The present results demonstrates that BNTM films are desirable lead-free ferroelectric materials for potential applications in integrated electronic devices.

2. Experimental details

2.1. Fabrication of BNTM100x ($0 \leq x \leq 10\%$) films

$Bi_{0.5}Na_{0.5}Ti_{1-x}Mn_xO_{3-\delta}$ (BNTM100*x*, $x = 0$, 2%, 4%, 6%, 8% and 10%) films on Pt(111)/Ti/SiO_2/Si(100) substrates were fabricated by a modified sol-gel technique. Analytically pure bismuth nitrate [$Bi(NO_3)_3 \cdot 5H_2O$, 99.0%], sodium acetate anhydrous (CH_3COONa, 99.0%), manganese acetate [$(CH_3COO)_2Mn \cdot 4H_2O$, 99.0%] and titanium butoxide ($Ti[O(CH_2)_3CH_3]_4$, 98.0%) were used as starting materials for (Bi, Na, Ti and Mn)-precursor solution. Acetic acid (CH_3COOH, 99.5%) and ethylene glycol ($C_2H_6O_2$, 99.0%) with a volume ratio of 2:1 were selected as the solvents. To prepare BNTM100*x* films, $Bi(NO_3)_3 \cdot 5H_2O$, CH_3COONa and $(CH_3COO)_2Mn \cdot 4H_2O$ were mixed in desired stoichiometric proportion, and then dissolved to obtain homogeneous, stable and transparent solutions after magnetic stirring in a certain temperature bath. In order to compensate for the volatile Bi loss during thermal annealing, excess bismuth of about 5 mol% was introduced into the precursor solutions. The sol was stabilized by adding an appropriate amount of acetylacetone ($C_5H_8O_2$, 99.0%). Subsequently, the required amount of $Ti[O(CH_2)_3CH_3]_4$ was also introduced into the mixture, and then the concentration of final solutions was adjusted to 0.3 M. Finally, the (Bi, Na, Ti and Mn)-precursors have been aged for 30 days in air to complete transformation of the sol to gel through hydrolysis and polycondensation reactions with atmospheric moisture.

Because of the favorable lattice match and platinum layer being directly bottom electrode for the electrical performance measurements or further applications, Pt(111)/Ti/SiO_2/Si(100) can be regarded as a suitable substrate. Firstly, the substrates with square dimension of about 15×15 mm^2 were cleaned in pure acetone and ethanol by ultrasonication to remove organic substances from the surface. Then, the substrates were rinsed repeatedly with deionized water and dried in a pure nitrogen stream before the film deposition. Furthermore, the stable precursor solutions were deposited by spin-coating process onto the Pt(111)/Ti/SiO_2/Si(100) substrates at a speed of 3700 rpm for 20 s. Each layer of the films was dried at 200 °C for 200 s on a hot plate in order to evaporate the solvent, and then subsequently pyrolyzed at 400 °C for 200 s to eliminate the residual organic components, followed by annealing at 650 °C for 200 s in ambient air to complete crystallization by a rapid thermal annealing procedure. Finally, the BNTM100*x* films were prepared by repeating eight times of the deposition and heating cycle to achieve the desired thickness.

2.2. Characterization methods

Crystalline microstructure and distortion of the BNTM100*x* films were investigated by X-ray diffraction (XRD) using a Ni filtered Cu $K\alpha$ radiation source (D/MAX-2550 V, Rigaku Co.) The surface morphology and domain patterns were recorded by atomic force microscopy (AFM: Digital Instruments Icon, Bruker) in a ScanAsyst mode and piezoresponse force microscopy (PFM), respectively. The cross-sectional images were observed by the field emission scanning electron microscopy (FESEM: Philips XL30FEG). X-ray photoelectron spectroscopy (XPS) measurements were carried out on a RBD upgraded PHI-5000C ESCA system (Perkin-Elmer) with Mg $K\alpha$ radiation ($h\nu = 1253.6$ eV). Raman scattering measurements were carried out using a micro-Raman spectrometer (Jobin-Yvon LabRAM HR 800UV) with a 532 nm laser taken as an exciting source. The ellipsometric spectral measurements were carried out using a near-infrared to ultraviolet (NIR-UV) spectroscopic ellipsometer in the wavelength range of 190–1100 nm with a spectral resolution of 5 nm (V-VASE by J. A. Woollam Co., Inc.). Platinum (Pt) dots with a diameter of about 0.2 mm deposited by a sputtering technique using a shadow mask are used as top electrodes for electrical measurements. And the Pt substrates are served as bottom electrodes. The polarization hysteresis loops were acquired by a ferroelectric test system (Precision Premier Π: Radiant Technologies Inc.). The leakage current-voltage (I-V) characteristics were measured using an electrometer (Keithley 6517A). Finally, dielectric behavior were recorded using a dielectric analyzer (BDS40, Novocontrol Tech.).

3. Results and discussion

3.1. Microstructure analysis

XRD patterns of the BNTM100*x* films with different Mn compositions in the 2θ range of 20–60° are shown in Fig. 1(a). A strong (110) and other weak (100), (200), (211) diffraction peaks are labeled in terms of pseudocubic cell since they are singlet. It indicates that all of the films are polycrystalline with pure single-phase perovskite structure. There is no secondary phase such as a more easily generated pyrochlore phase of $Bi_2Ti_2O_7$ deteriorating the electrical properties severely, which can be ascribed to

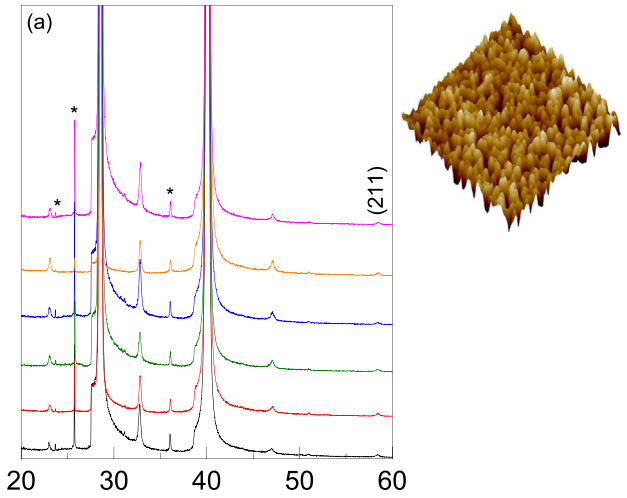

Fig. 1. (a) XRD patterns of the BNTM100*x* ($x = 0$, 2%, 4%, 6%, 8% and 10%) films grown on Pt(111)/Ti/SiO_2/Si(100) substrates. The peaks marked by the asterisk symbol (∗) originate from substrates. (b)Three-dimensional AFM with the measured area of $1 \times 1\ \mu m^2$ and (c) the cross-sectional SEM image of the BNTM10 film. Note that the Miller indices are labeled in terms of pseudocubic cell for a convenient reading.

restraining the nonstoichiometric defects and favorable annealing condition. It is evident that the position of all the diffraction peaks appear unconspicuous shifting with increasing Mn composition due to the almost equal ionic radius of Ti^{4+}(0.61 Å) compared to that of Mn^{3+}(0.65 Å). As can be seen from these patterns, broadenings (β) and intensity of all the diffraction peaks show little change, which indicates that the grain size of samples has no significant change. Moreover, all the (110) diffraction peaks are singlet because the annealing was carried out at about 650 °C. It is much lower than 1200 °C, at which the (110) profile will appear as a triplet [28]. These phenomena reveal that Mn is completely incorporated into the BNT host lattice and it does not transform the original phase structure. Based on the (110) diffraction peak, the lattice constant *a* of BNTM100*x* films in terms of pseudocubic cell is various from 3.8511 to 3.8581 Å, as list in Table 1. The differences of lattice constants mean that there are varied degrees of distortion in the lattice. The grain size *r* was derived from the (110) diffraction peak according to the well-known Scherrer's equation, where the grain size (~32.3 nm) of the BNTM2 film is the smallest due to the largest broadening (β). The detailed information about film crystal structure are listed in Table 1.

The three-dimensional AFM images of BNTM100*x* films suggests a similar pattern (e.g., Fig. 1(b) for BNTM10). The root-mean-square (RMS) values of the surface morphology are 3.06, 4.59, 4.78, 5.52, 4.19 and 3.98 nm for Mn concentration of 0, 2%, 4%, 6%, 8% and 10%, respectively. In addition, Fig. 1(c) shows a cross-sectional SEM image of the BNTM10 film. There is an obvious interface between the film and Pt substrate, which suggests that all films are crack-free, uniform and compact. With regard to the XRD patterns, surface morphology images, and SEM imagines, all films are well crystallized and highly homogeneous.

Table 1
Position (2θ) and broadening (β) of the diffraction peak (110) in terms of pseudocubic cell as well as related structure information of BNTM100*x* films.

Samples	(110)		*a*	*r*
	2θ(°)	β(°)	(Å)	(nm)
BNTM0	32.789	0.257	3.8581	34.9
BNTM2	32.848	0.275	3.8514	32.3
BNTM4	32.810	0.248	3.8557	36.5
BNTM6	32.810	0.270	3.8557	33.0
BNTM8	32.849	0.268	3.8512	33.2
BNTM10	32.850	0.258	3.8511	34.8

3.2. Valence states of Mn ions in BNTM100*x* films

The chemical states of Mn ions in BNTM100*x* films were detected by a XPS technique. As an example, Fig. 2 illustrates a overall core level XPS survey spectrum of the BNTM8 film, which indicates that Bi 5d, Bi 4f, C 1s, Ti 2p, O 1s, Mn 2p and Na 1s related core levels were observed. In order to analyze the chemical bonding states, the Mn 2p core level XPS spectra are plotted in the inset Fig. 2(a), where the peaks became more pronounced with increasing Mn composition. The XPS data fitted by 20% Lorentzian and 80% Gaussian functions are plotted in the inset Fig. 2(b). Note that the binding energy are located at 653.5 eV and 641.9 eV for Mn $2p_{1/2}$ and Mn $2p_{3/2}$ states, respectively. The XPS results demonstrate that Mn element is introduced into the lattice and Mn^{3+} ions exist in the BNTM100*x* films.

3.3. Raman scattering

According to group theory, zone-center optical phonon modes of the rhombohedral phase (*R*3*c*) for BNT are classified into $4A_1 + 9E + 5A_2$, where the optical non-degenerate A_1 and doubly degenerate E modes are both infrared and Raman active [29]. Note that the A_2 modes turn silent ones when A-site disorder is taken into consideration [8]. The phonon wave vector of A_1 modes is related to lattice displacements along the *z*-axis of the unit cells, while the oscillator strength vector of E modes associates with phonon propagating belong to the *x*-*y* plane [30]. Generally, the modes below 150 cm^{-1} are dominated by displacement of Bi ions and the ones in the frequency range of 155–187 cm^{-1} are related to Na-O vibrations [29]. The bands between 200 and 450 cm^{-1} involve vibrations of Ti-O bonds and ones in the high wavenumber range of 450–1000 cm^{-1} are associated with vibrations and/or rotations of TiO_6 octahedra. In order to eliminate the contribution from the Bose-Einstein population factor, all measured Raman spectra were modified by the Bose-Einstein temperature factor.

Raman spectra of the BNTM100*x* films measured at room

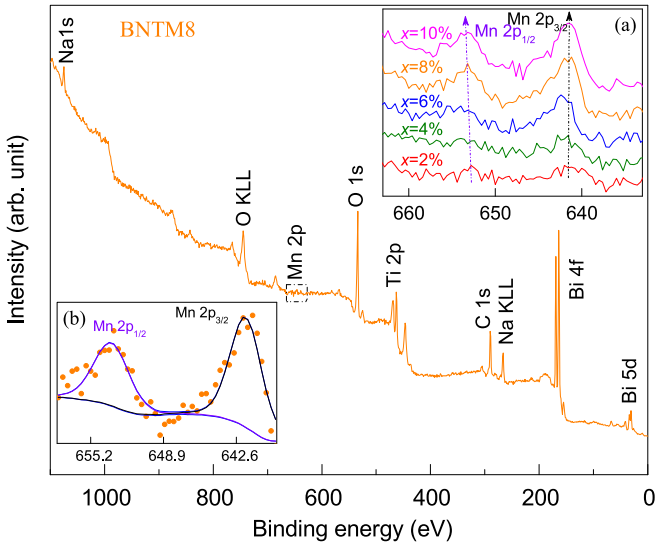

Fig. 2. Overall core level XPS spectrum of the BNTM8 film. (a) Enlarged Mn $2p_{3/2}$ and $2p_{1/2}$ spectra of BNTM100*x* films with different Mn concentrations. (b) Experimental (dotted lines) and fitting (solid lines) XPS spectra of Mn 2p states in the BNTM8 film.

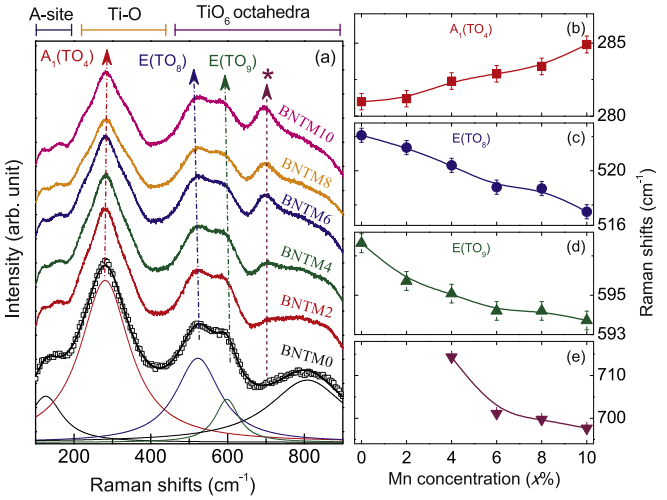

Fig. 3. (a) Room-temperature Raman spectra and mode assignments of the BNTM100*x* ($x = 0$, 2%, 4%, 6%, 8% and 10%) films. The arrows indicate various trends of the phonon frequencies at about 282, 520, 595 and 700 cm^{-1}, The Raman modes (b) $A_1(TO_4)$, (c) $E(TO_8)$, (d) $E(TO_9)$, and (e) an additional mode as a function of Mn concentration.

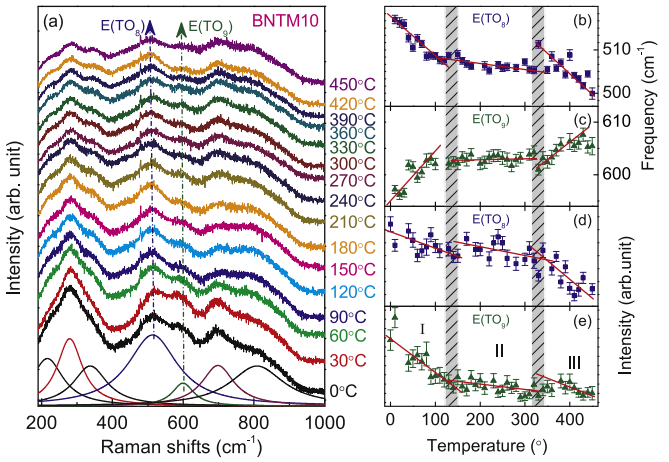

Fig. 4. (a) Raman spectra of the BNTM10 film measured in the temperature range of 0–450 °C. For clarity, each spectrum is shifted in intensity. The various (b, c) frequency and (d, e) corresponding intensity of E(TO..) and $E(TO_9)$ Raman-active modes as a function of temperature. The solid lines are a guide for the eyes to emphasize the various trends and the shaded stripes are applied to show the boundaries of adjacent phases.

temperature are shown in Fig. 3(a), which is in good agreement with reported BNT-based ferroelectrics [5,8,9]. There is no obvious splitting into doublet or multi peaks near 300 cm^{-1}, which indicates that there is no phase transition [31]. Besides, the relatively broadening phonon bands near 300 cm^{-1} could be ascribed to the B-site disorder caused by Mn^{3+} introduction, which is similar to that of the dysprosium-modified BNT system [32]. Notable changes are observed near 700 cm^{-1} where an obvious peak (∗) appears with increasing Mn composition. It unquestionably suggests that Mn ions are incorporated successfully into lattice and increases the structural asymmetry. Furthermore, all Raman spectra were fitted with Lorentzian-shaped deconvolution, and the evolution of composition-dependent main modes is depicted in Fig. 3(b–e). The mode near 280 cm^{-1} has a slightly shift towards to higher wavenumber with increasing Mn composition. The substitution by larger radius Mn^{3+} ions results in an expansion of unit cells, which benefits the displacement of Ti^{4+} and leads to higher wavenumber. Whereas, the opposite shifts are observed in the region between 450 and 700 cm^{-1}. The changes in the region are related to the octahedron-tilt-related distortions, which are caused by the stretching and bending of MnO_6 (Ti^{4+} substitution by Mn^{3+} ions) octahedra [33]. It can be concluded that Mn ions are substituted at the B-site Ti ions and promote the off-center displacement of Ti ions, which induces lattice structure distortion and benefits the polarization.

To explore the temperature-driven phase transitions of BNTM100*x* films, Raman spectra were recorded in the temperature range of 0–450 °C. Fig. 4(a) shows the temperature-dependent Raman spectra of BNTM10 film as a representative. As temperature increases, the Raman modes in the range of 450–650 cm^{-1} gradually become weaker and broadening is observed, which indicates the increase of structural symmetry. Thus, special attention has been paid to the first-order Raman-active modes $E(TO_8)$ and $E(TO_9)$ for extracting the transition temperature. All the Raman spectra were decomposed into a series of bands with the multi-Lorentzian oscillator approximation. Fig. 4(b–e) show the temperature-dependent frequency and intensity of modes, which are related to oxygen octahedral rotations/vibrations. An opposite shift of the vibration modes near 510 and 600 cm^{-1} against temperature are observed, which are mainly attributed to the lattice thermal expansion and anharmonic multiphonon coupling, respectively. The perturbation model can express the phonon frequency as a function of temperature, which is written as [34]: $\omega(T) = \omega_0 + \Delta\omega_e(T) + \Delta\omega_d(T)$, here $\Delta\omega_e(T) = -\omega_0\gamma\int_0^T[\alpha_a(T) + \alpha_b(T) + \alpha_c(T)]dT$, $\Delta\omega_d(T) = A[1 + 2/(n_1 - 1)] + B[1 + 3/(n - 1) + 3/(n - 1)^2]$+ higher order terms. Here, $n_1 = \exp(\hbar\omega_0/2k_BT)$, $n = \exp(\hbar\omega_0/3k_BT)$, γ is Grüneisen parameter, α_a, α_b, and α_c are the thermal expansion coefficients in the *a*, *b*, and *c* axis, respectively. The first term is associated with the harmonic frequency of optical mode, the second one corresponds to the lattice thermal expansion, and the third one is related to cubic, quadratic, and higher order anharmonic coupling between multiphonon. Therefore, the thermal expansion and anharmonic multiphonon coupling mainly lead to the redshift and blueshift of mode frequency with increasing temperature, respectively. A further step, the visible deviation from linearity for the frequency and intensity of modes are observed, which suggests that there are two phase transitions ($T_1 \sim 200$ °C and $T_2 \sim 350$ °C for BNTM4, and $T_1 \sim 130$ °C and $T_2 \sim 330$ °C for BNTM10) in the temperature range of 0–450 °C. It has been reported that subtle changes of Raman modes in $Bi_{0.5}Na_{0.5}TiO_3$-$Bi_{0.5}K_{0.5}TiO_3$ and $Bi_{0.5}Na_{0.5}TiO_3$-$BaTiO_3$ indicate the phase transitions from ferroelectric (F) to antiferroelectric (AF) to paraelectric (PE) [8,31]. Therefore, the two anomaly temperature can be regarded as the F → AF → PE phase transitions in BNTM100*x* films.

3.4. Ellipsometric spectra

Specifically, SE measures the relative changes in the amplitude $\Psi(E)$ and phase $\Delta(E)$ of particular directions polarized lights upon oblique reflection from sample surface [18,35]. In order to extract simultaneously optical dielectric functions [$\tilde{\varepsilon}(E) = \varepsilon_r(E) + i\varepsilon_i(E)$] and thicknesses of multilayer films, the SE spectra were analyzed by a multilayer model with a four-phase layered structure (air/surface rough layer (SRL)/BNTM100*x* film/Pt substrate). $\Psi(E)$ and $\Delta(E)$ are functions of incident angle, optical constants, film thickness, photon energy, etc. Generally, the complex dielectric function is associated with interband electronic transitions. The Adachi dielectric function model is chosen to express the dielectric dispersion of the BNTM100*x* films from the transparent to strong absorption region based on the Kramer-Kröning transformation (KKT). The model is related to electronic band structure and it

reveals the distinct structures at the energy of the M_1-type critical point, which is expressed as [36]: $\tilde{\varepsilon}(E) = \varepsilon_\infty - A_0 \ln(1 - \chi_0^2)/\chi_0^2$. Where, $\chi_0 = (E + i\Gamma_0)/E_g$, A_0 and Γ_0 are the strength and broadening of the optical band gap (E_g), respectively. The high frequency dielectric constant ε_∞, band gap E_g, thicknesses of films (d_f) and SRL (d_s) could be extracted by fitting experimental spectra perfectly. Moreover, the well-known relationships [$\tilde{N}(E) = n(E) + i\kappa(E)$] and $\tilde{N}(E) = \sqrt{\tilde{\varepsilon}(E)}$ include the information of optical constants containing refractive index (n) and extinction coefficient (κ). The Brüggeman effective medium approximation was applied to calculate the contribution from dielectric functions of SRL, where its value was selected as a mixture of 50% void and 50% film. The fixed mixture ratio is acceptable due to the negligible deviation.

Fig. 5(a) and (b) depict the experimental and fitted ellipsometric spectra [$\Psi(E)$ and $\Delta(E)$] of the BNTM100x samples. It suggests that the experimental and fitted spectra reach a good agreement in the entirely measured photon energy range, which means that the Adachi model used to describe the dielectric dispersion behavior of BNTM100x films is reasonable. Additionally, the fitted model parameter values are summarized in Table 2. The interference patterns owing to the multi-reflectance between two sides of film are observed at the photon energy below 3.5 eV, which indicates that the films are transparent in the low energy region. The evolution of n with the photon energy has a typical optical dispersion behavior (Fig. 5(c)). With increasing photon energy, n increases and reaches the maximum at about 3.95 eV, and then decreases owing to the well-known Van Hove singularities. In the transparent region ($E < E_g$), the extinction coefficient κ is close to zero, and then remarkably increases as the photon energy further increases beyond the fundamental band gap (Fig. 5(d)), which indicates that a strong optical absorption appears. Furthermore, the absorption edges of BNTM100x films with different Mn compositions have not a remarkable change. Correspondingly, the optical band gap E_g almost the same after the Mn-doping, even though the average value (~3.96 eV) is larger than those of Ce-doped BNT (~3.28 eV) and theoretical prediction (~3.03 eV) [11,16]. Therefore, the Mn substitution cannot significantly effect on the electronic band structure of BNT films. Note that there is no phase transition combined with the room-temperature XRD and Raman analysis.

Table 2
Parameter values of the Adachi dielectric function model for BNTM100x films determined from the simulation of ellipsometric spectra.

Samples	C_{Mn} (%)	ε_∞	A_0 ($eV^{1.5}$)	Γ_0 (eV)	E_g (eV)	d_s (nm)	d_f (nm)
BNTM0	0	1.26	3.96	0.095	3.949	4	172
BNTM2	2	1.22	3.54	0.114	3.950	3	184
BNTM4	4	1.13	3.74	0.152	3.962	5	182
BNTM6	6	1.03	4.01	0.165	3.984	9	176
BNTM8	8	1.10	3.69	0.183	3.961	3	189
BNTM10	10	1.55	3.82	0.195	3.947	5	171

Theoretically, the top of valence bands (VB) are mainly derived from O-2p, Ti-3d and Bi-6p states, which presents a strong hybridization between O-2p and Ti-3d/Bi-6p. The Bi-6s states occupy lower energy bands of the VB. On the other hand, the bottom of conductive bands (CB) of BNT mainly come from Ti-3d, Bi-6p, and Na-2s states. The higher energy bands mainly correspond to the strong mixture of Na-2p and Bi-6p orbits with minor contributions from O-2p states. It should be emphasized that the maximum of VB at the Γ-point are mainly occupied by O-2p states and the minimum of CB at the Γ-point are dominated by the Ti-3d and Bi-6p states, which suggests that BNT has a direct optical band gap [11,16,29]. Thus, the fundamental electron transitions at the Γ-point from O-2p states to Ti-3d/Bi-6p ones determine the electric and optical properties.

To further investigate the temperature-driven evolution of electronic band structure and confirm the intermediate phase transition of BNTM100x films, temperature-dependent ellipsometric spectra have been recorded from 0 to 450 °C upon heating. As an example, Fig. 6(a) displays the experimental ellipsometric spectra $\Psi(E)$ and $\Delta(E)$ of the BNTM10 film measured at 0 and 450 °C. There are obvious distinctions from raw experimental data. The derived complex dielectric functions in the photon energy range of 1.2–5.5 eV with increasing temperature are revealed in Fig. 6(b). The optical constants n and κ still exhibit typical optical dispersion behavior with increasing photon energy and temperature. The imaginary part κ spectra near the absorption edge have a

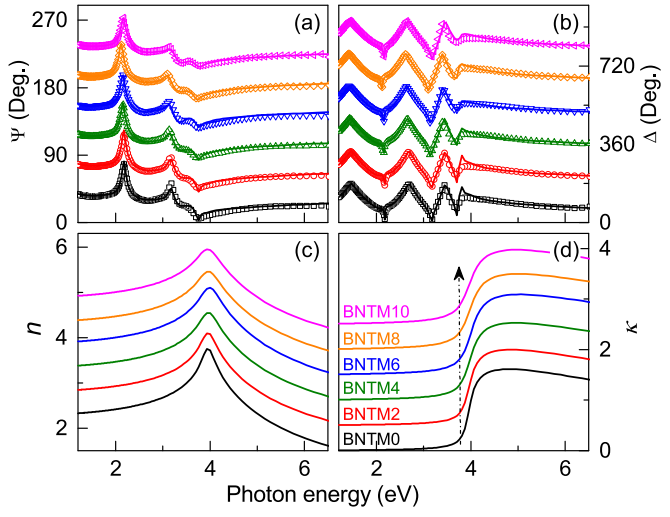

Fig. 5. NIR-UV experimental (dotted lines) and best-fitted (solid lines) ellipsometric spectra (a) $\Psi(E)$ and (b) $\Delta(E)$ of the BNTM100x films. The corresponding (c) refractive index n and (d) extinction coefficient κ of the BNTM100x films. The arrow indicates absorption edges.

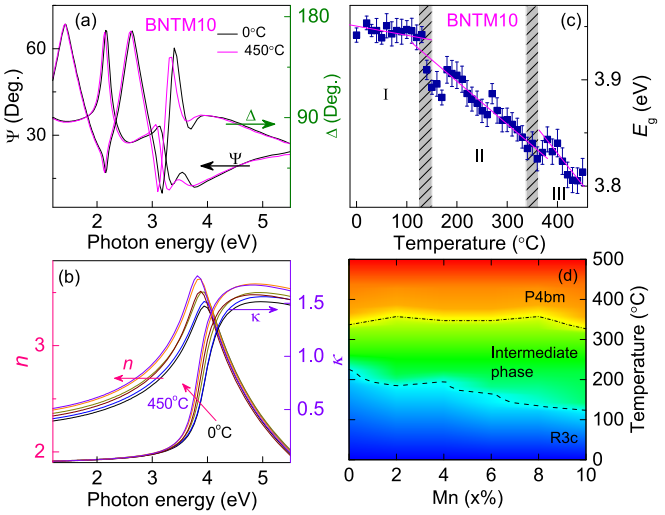

Fig. 6. (a) NIR-UV experimental ellipsometric spectra $\Psi(E)$ and $\Delta(E)$ of the BNTM10 film measured at 0 °C and 450 °C. (b) The evolution of refractive index (n) and extinction coefficient (κ) of the BNTM10 film with increasing temperature. (c) Optical band gap E_g for BNTM10 film as a function of temperature. (d) Phase diagram of BNTM100x films with different Mn compositions based on the SE and Raman scattering analysis.

remarkable redshift trend with increasing temperature and there is an abrupt variation near 100 and 300 °C. As temperature rises, the temperature effect stemming from the lattice thermal expansion and electron-phonon interaction begins to take effect by altering the interatomic distance along their arrangement direction via longitudinal phonons, which ultimately induces the CB down and the VB up [5]. The abrupt variation signifies the various electronic band structure. To clarify the extraordinary temperature points and confirm the Raman results, the E_g of the BNTM10 film was plotted as a function of temperature (Fig. 6(c)). The interrupts of slope occur near 130 and 330 °C. Therefore, the variations of E_g divides the temperature range into three regions, which are consistent with the results from Raman scattering. The ferroelectric phase transition is closely connected with interband electronic transition energy. As mentioned above, Ti-3d (Mn-3d) and O-2*p* orbits mainly govern the CB bottom and VB top, respectively. As phase transition proceeds from ferroelectric to anti-ferroelectric to paraelectric, the off-center B-site cations will move smoothly to the center position of BO_6 octahedra. The shifting of B-site cations influence the interatomic orbital hybridization in BO_6 octahedra, which results in abnormal variation of E_g. Thus, the abrupt variation can provide evidence for structural transformations and phase transformation combining with the Raman scattering. According to previous research, the *in situ* temperature-dependent transmission electron microscope study on BNT crystals demonstrates a direct link between structural variation and electrical ordering. There is a phase transition from ferroelectric rhombohedral (*R*3*c*) to paraelectric tetragonal (*P*4*bm*) phase through an intermediate antiferroelectric modulated phase. It is established experimentally that these transitions correlate with approximate rotations/tiltings of BO_6 octahedra and the cation displacement alone the corresponding direction. The occurrence of different octahedra tilting conditions under a single network suggests the competition between the two incompatible order parameters, which results in an intermediate modulated phase [37,38]. Thus, it is reasonable to identify the various trends of Raman modes and E_g as a function of temperature illustrate the phase transitions. An acceptable sequence of phase transitions, *R*3*c* → the intermediate modulated phase → *P*4*bm*, are deduced in BNTM100*x* films upon heating. The two phase transitions (T_1 and T_2) between *R*3*c* and *P*4*bm* in Mn doping BNT films have been extracted to about 230 and 340 °C for BNTM0, 190 and 360 °C for BNTM2, 200 and 350 °C for BNTM4, 170 and 350 °C for BNTM6, 140 and 360 °C for BNTM8, and 130 and 330 °C for BNTM10. Based on the present spectroscopic results and previous research about BNTM system, the phase diagram of BNTM100*x* with a intermediate modulated phase has been obtained, as shown in Fig. 6(d). Instead of the traditional electrical experiments, the spectroscopic optical method opens a new window for exploring the phase diagram. It would be meaningful for BNT-based future applications related to phase transition in the relevant operating temperature range.

3.5. Ferroelectric performance of BNTM100x films

The typical polarization-electric field (*P*-*E*) ferroelectric hysteresis loops of Pt/BNTM100*x*/Pt capacitors were measured at room temperature with a test frequency of 1 kHz (Fig. 7a and b for pure and 10% Mn-doping). The optimal ferroelectric performance is obtained when Mn concentration reaches 10% for BNTM100*x* films based on the shape of *P*-*E* loops, P_r values, and dielectric breakdown voltage. Since Mn^{3+} ionic radius is larger than that of Ti^{4+}, the introduction of Mn^{3+} ions leads to increase of dipole size and larger off-center displacement of B-site ions, which promotes the polarization. What's more, the structure distortions and improvement of structural asymmetry also contribute to the polarization. Moreover, the mobile charge carriers or defects tend to move towards domain walls and eventually pin the domain walls, leading to hindering the domain wall motion and degradation of switching. Such the "domain wall pinning effect" significantly affects ferroelectric properties. Mn-dopant can reduce oxygen vacancies concentration to enhance the effect. In addition, all the *P*-*E* loops have a tendency toward negative electric field. The E_{C-} value is larger than that of E_{C+} (E_{C-} is about 241 kV cm^{-1}, while E_{C+} is about 168 kV cm^{-1} for the BNTM10 at the electric field of 1200 kV cm^{-1}). The asymmetric coercive field may be originated from two factors: (i) the mechanical stress is formed during the thermal process, which can contribute to the preferential orientation of ferroelectric domains [39]; (ii) the formation of defect complexes (such as $V_O^{2-} - V_{Bi}^{3+}$ or $MnTi' - V_O^{2-} - MnTi'$) will lead to a local internal field (E_{loc}) toward top electrode [40]. It should be pointed out that positive electric field is defined as the electric field from bottom electrodes to top ones. Consequently, when the domains switch from positive to negative direction, it needs more energy to overcome E_{loc}, which results in a relative large applied electric field. Conversely, it is relatively easy to switch the domains from negative to positive states due to the assistance of E_{loc}. Moreover, the maximum value of P_r (~32.1 μC/cm^2) is larger than that of BNT-based films prepared by sol-gel deposition (~14.9 μC/cm^2) [16], pulse laser deposition (~11.3 μC/cm^2) [41] and radio-frequency magnetron sputtering (~11.9 μC/cm^2) [42], as shown in Fig. 7(c) and (d). Compared with BNT-based single crystals and ceramics, the as-deposited Mn-doped BNT films perform excellent ferroelectricity, which makes it possible to be used in the design of nonvolatile ferroelectric random-access memory (NVFRAM).

To further understand the ferroelectric nature and domain structure, PFM measurements are carried out in both lateral and vertical modes to analyze the domain patterns. Based on the reverse piezoelectric effect, the in-plane (IP) and out-of-plane (OP) signals can be obtained, whose polarization vector parallel and perpendicular to the film surface, respectively. The signals contain information about piezoresponse phase and amplitude. Fig. 7(e) and (g) show the IP phase images of the BNTM8 and BNTM10 films, respectively. It reveals that the clustered macro-domains distribute randomly and a clear domain contrast appears between distinct regions. The difference value of the phase between bright and dark regions is about 180°, suggesting that the 180° domain exists in the films. The domains in the BNTM10 film are more homogeneous as compared to those of BNTM8 films. In addition, the OP amplitude patterns indicate that there are opposite polarization in ferroelectric domains (Fig. 7f and h). The bright regions correspond to negative domains with the polarization oriented upward, while the dark regions related to positive domains with the polarization oriented downward. The IP and OP PFM images reveal the ferroelectric behavior and the dominance of 180° nano-domain structure.

Energy harvesting and storage have been becoming a hot topic in electronic devices field. Film-based capacitors are also crucial compared to other available energy storage devices (batteries, fuel cells, and super-capacitors). These capacitors usually possess higher energy density owing to their exceptionally quick charging-discharging rate [43]. For relaxor ferroelectrics, the electric energy storage density (*W*) can be calculated from the *P*-*E* hysteresis loops according to the expression [44]: $W = W_{rec} + W_{loss} = \int_0^{P_{max}} E \cdot dP$, $(0 \le E \le E_{max})$. Where W_{rec}, W_{loss}, *E* and *P* are the recoverable energy storage density, energy loss density, electric field and polarization, respectively. During the charging process, the polarization climbs to the maximum P_{max} with increasing electric field, and electric energy is stored in relaxor ferroelectrics. Conversely,

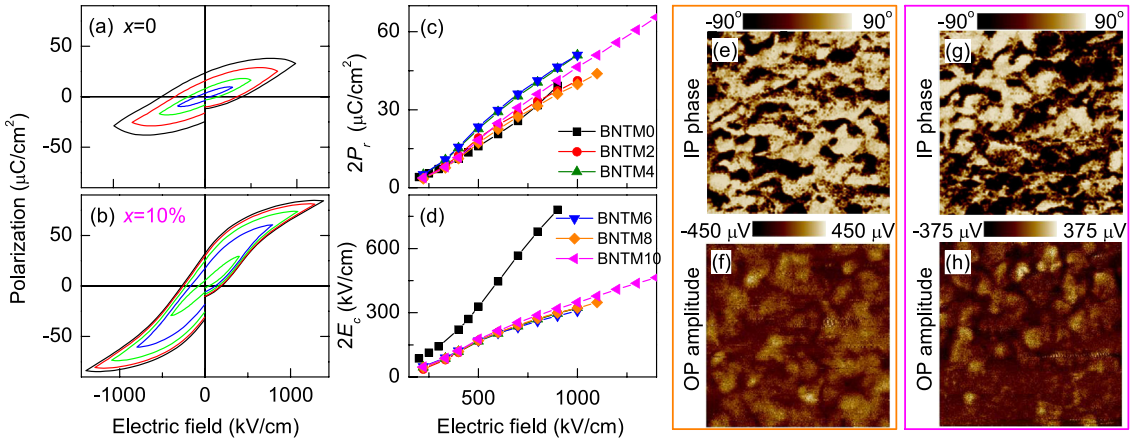

Fig. 7. Ferroelectric hysteresis loops (*P-E*) of (a) BNTM0 and (b) BNTM10 measured at $f = 1$ kHz and room temperature. The corresponding (c) $2P_r$ and (d) $2E_c$ of the BNTM100*x* films with different Mn concentrations. The in-plane (IP) PMF phase of (e) BNTM8 and (g) BNTM10 films. The out-of-plane (OP) PFM amplitude of (f) BNTM8 and (h) BNTM10 films.

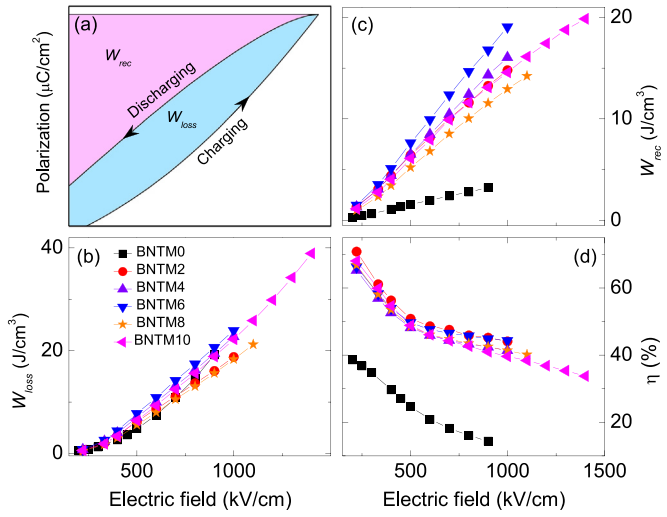

Fig. 8. (a) Schematic diagram of the energy storage properties of relaxor ferroelectrics. The calculated (b) recoverable energy storage density W_{rec}, (c) energy loss density W_{loss}, and (d) energy storage efficiency η of BNTM100*x* films as a function of applied electric field.

the recoverable energy storage density W_{rec} is released during the discharging process, represented by the light magenta area in Fig. 8(a). The W_{rec} can be estimated based on the relationship [44]:

$$W_{rec} = \int_{P_r}^{P_{max}} E \cdot dP, \quad 0 \le E \le E_{max}. \tag{1}$$

As a result, a portion of the stored energy is unrecovered owing to the hysteresis loss, which is called energy loss density W_{loss} (the light blue area in Fig. 8(a)). The energy storage efficiency η is estimated according to the equation:

$$\eta = \frac{W_{rec}}{W} = \frac{W_{rec}}{W_{rec} + W_{loss}} \times 100\%. \tag{2}$$

The *P-E* loops show that pure BNT films display a saturated loop, while Mn-doped BNT films exhibit a slim loop. Based on eqn (1), the doped BNTM100*x* films are more favorable for achieving higher W_{rec} because they simultaneously possess higher dielectric breakdown voltage, and larger polarization difference between P_{max} and P_r. Fig. 8 (b–d) illustrate the energy storage properties of BNTM100*x* films as a function of electric fields. The W_{rec} and W_{loss} show a linearly increasing trend with increasing electric field, and the W_{rec} are dramatically improved after Mn doping, while the W_{loss} show an unconspicuous variation. The largest W_{rec} of 19.84 J/cm^3 is obtained for BNTM10 films at 1400 kV cm^{-1}. Such a large W_{rec} of 19.84 J/cm^3 is superior to the values reported for BNT-based ceramics [45,46]. The improvement of W_{rec} could be briefly explained from two aspects: (a) large dielectric breakdown voltage leading to a large P_{max}, which are beneficial for W_{rec}; (b) the increase of polarization and dielectric constant (demonstrated as follows) are conducive to W_{rec}. Nevertheless, the η declines from 68.1% to 34% with electric fields increasing from 220 to 1400 kV cm^{-1} for BNTM10, which originates from the high W_{loss} in the high electric field region. The η substantially increases accompanied by Mn substitution. Therefor, the doped BNTM100*x* films are desirable materials for high energy storage capacitors.

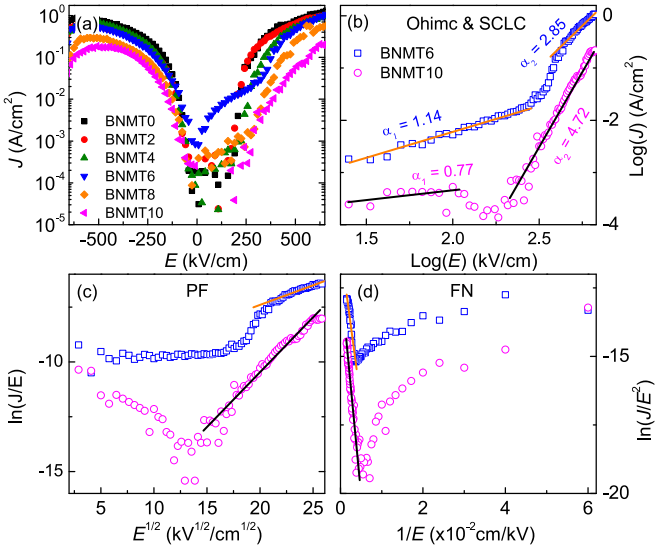

Fig. 9. (a) *J-E* curves of BNTM100x films with different Mn concentration. (b) log(*J*)-log(*E*), (c) ln(*J*/*E*)-$E^{1/2}$, and (d) ln(*J*/E^2)-1/E of BNTM6 and BNTM10 films. Note that different fits of these data are applied to determine the leakage mechanism of BNTM100*x* films and the parameter α is slope.

3.6. Leakage current mechanisms of BNTM100x films

Fig. 9(a) shows the room temperature leakage current density (J) of BNTM100x capacitors as a function of applied electric field (E). There is an optimal Mn concentration of 10%, whose insulation property reaches the best performance. It is generally accepted fact that the generated space charges (such as oxygen vacancies) are one of major source of leakage current. Bi^{3+} and alkali Na^{+} ions are easy to volatilize (↑) during the heat treatment process as described by the following actions:

$$2Bi^{3+} + 3O^{2-} \rightleftharpoons Bi_2O_3(g)\uparrow + 2V_{Bi}^{3-} + 3V_O^{2+}, \quad (3)$$

$$2Na^{+} + O^{2-} \rightleftharpoons Na_2O(g)\uparrow + 2V_{Na}^{-} + V_O^{2+}. \quad (4)$$

Simultaneously, the next reaction will take place [22].

$$4Ti^{4+} + 2O^{2-} \rightleftharpoons 4Ti^{3+} + O_2\uparrow + 2V_O^{2+}. \quad (5)$$

Thus, the oxygen vacancies will produce sharply during the pyrolysis process. Consequently, the ion vacancies and oxygen vacancies will coexist. The oxygen vacancies can move easily with high mobility resulting in leakage current. Moreover, the oxygen occupies oxygen vacancies accompanied by the formation of free carrier holes, which can be explained by the following equation:

$$1/2O_2 + V_O^{2+} \rightleftharpoons O^{2-} + 2h^{\bullet}. \quad (6)$$

These holes have higher mobility than that of oxygen vacancies. Whereas, the substitution of Mn can effectively decrease the concentration of oxygen vacancies by absorbing holes, which can be expressed by the reaction:

$$Mn^{2+} + h^{\bullet} \rightleftharpoons Mn^{3+}. \quad (7)$$

The absorbing of holes will promote the balance of eqn (6) to the right side. Combining with eqns (5)–(7), we gain the total reaction:

$$Ti^{4+} + Mn^{2+} \rightleftharpoons Ti^{3+} + Mn^{3+}. \quad (8)$$

From eqn (8), the oxygen vacancies and holes are avoided. Furthermore, Mn^{3+} ions induce $MnTi' - V_O^{2-} - MnTi'$ defect complexes between acceptors and oxygen vacancies. The electric field required for generating mobile oxygen vacancies would be increased since it needs more electric energy to overcome the electrostatic attraction force of defect complexes. That is to say, the defect complexes limit free movement of oxygen vacancies and effectively depress mobility.

In order to further analyze leakage mechanisms of BNTM100x films, several conduction mechanisms can be divided into certain regions: ohmic conduction, space-charge-limited conduction (SCLC), Poole-Frenkel emission (PF), and Fowler-Nordheim tunneling (FN) [33,47,48]. The ohmic conduction mechanism can be expressed by the following equation: $J = nq\mu E$, where n, q and μ are carrier concentration, electron charge and carrier mobility, respectively. Fig. 9(b) shows that the slope near 1 means the J versus E curve is in general accord with a straight line, coming to the conclusion that the ohmic conduction mechanism is considered as a possible current transport mechanism of BNTM100x films in the low electric field region. At room temperature, the electron concentration produced by thermal excitation is very low because of large band gap. Furthermore, electrons are rarely injected into film via electrode on account of low electric field. In addition, the SCLC mechanism originates from the electric field derived from free carriers. These free carriers from electrode are trapped by defects in films, generating the electric field opposite to applied electric field. The current density for SCLC can be described by the relationship: $J_{SCLC} = 9\mu\varepsilon_0\varepsilon_r E^2/8d$, where ε_0, ε_r and d are dielectric constant of free space, relative dielectric constant and thickness of film, respectively. The slopes are not close to 2 in high electric field, indicating that the leakage mechanism against the SCLC in this region. Fig. 9(c) shows the $\ln(J/E)$ *versus* $E^{1/2}$ curve based on the equation of the PF: $J_{PF} = CE\exp[-(E_I - q\sqrt{qE/(\pi\varepsilon_0\kappa)})/(\kappa_B T)]$, where C is a constant, E_I is the trap ionization energy, κ is the optical dielectric constant, and κ_B is the Boltzman constant. This phenomenon originates from the field induced excitation of trapped carriers into the CB. The PF model can be excluded due to the incompatible optical dielectric constant. Additionally, interface-limited FN model can be expressed as $J_{FN} = CE^2\exp[-D^2\sqrt{\varphi^3}/E]$, where $C = q^2/(8\pi h\varphi)$, $D = -8\pi\sqrt{2qm^*}/(3h)$, h is the Plank's constant, φ is the potential barrier height, and m^* is the effective mass. Owing to the narrowed oxide energy barrier width, the FN model is related to the leakage mechanism at high electric field. The $\ln(J/E^2)$ *versus* $1/E$ curve suggests that the FN model can be regarded as a possible leakage mechanism at high electric field, as shown in Fig. 9(d). In a word, the introduction of Mn can reduce the leakage current density by diminishing oxygen vacancies/holes concentration and forming defect complexes. It is found that the ohmic conduction mechanism is dominating leakage process in the low electric field region, while the FN model is regarded as the primary current transport mechanism in the high electric field region.

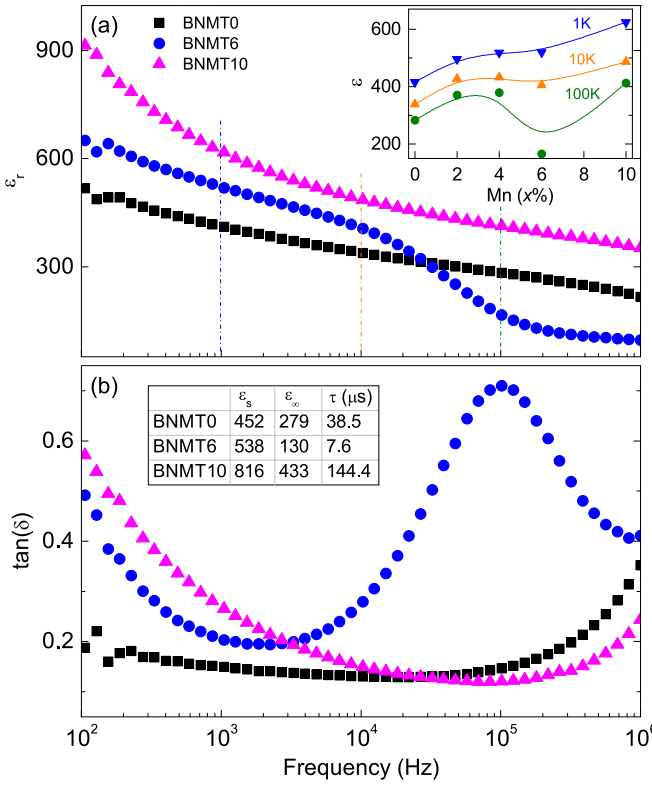

Fig. 10. Frequency-dependent (a) real part of relative dielectric constant ε_r and (b) dielectric loss $\tan(\delta)$ of BNTM0, BNTM6 and BNTM10 films measured at room temperature. The inset of (a) depicts the corresponding ε_r of BNTM100x films at 1 KHz, 10 KHz, and 100 KHz. The table in (b) lists the static (ε_s) and high frequency (ε_∞) dielectric constants as well as relaxation time (τ) of BNTM100x based on the Debye model.

3.7. Dielectric properties of BNTM100x films

In order to deepen knowledge about the Mn-doping effect on dielectric performance, the relative dielectric constant ε_r and dielectric loss tan(δ) as a function of frequency ranging from 100 Hz to 1 MHz are measured at room temperature. Fig. 10(a) shows the real part of relative dielectric constant of films with $x = 0$, 6 and 10 as examples. It suggests that the dielectric constant decreases gradually with increasing frequency, which indicates that the dielectric relaxation type behavior appears [15]. The dielectric dispersion can be explained by Koop's theory, in which the essence is that establishment of polarization requires a certain time [49]. In other words, polarization may not be able to keep pace with changes of applied electric field as frequency increases due to the presence of hysteresis or axial inertia of ferroelectric capacitors. Usually, dielectric constant depends on the polarization of substance under applied electric field. In low frequency region, polarization can respond to frequency of applied electric field without delay, which causes the maximum value of dielectric constant. The decrement of dielectric constant with increasing frequency is attributed to the decreased contribution of polarization (electron and ion displacement polarization) at elevated frequency. In the low frequency region, Mn substitution increases dielectric constant as shown in the inset of Fig. 10(a), which indicates that Mn substitution is conducive to polarization and improves performance of film capacitor in charge-storage. Fig. 10(b) shows dielectric loss *versus* frequency for BNTM0, BNTM6 and BNTM10 as representatives. Interestingly, the dielectric loss appears enormously different in relative high frequency region. Most literatures illustrate dielectric loss behavior as BNTM0 and BNTM10 perform and the peculiar phenomenon in BNTM6 is rarely recorded. The dielectric loss chiefly stems from two factors: dielectric leakage and polarization relaxation. The leakage current is inevitable in ferroelectric capacitors while polarization relaxation also exist as discussed above. Noted that polarization relaxation behavior can be approximately neglected in relative low frequency region so that the ferroelectric capacitor can be regarded as ideal plate capacitor. Based on physical knowledge, dielectric loss can be expressed by the following equation: $\tan\delta = I_R/I_C = G/(C\cdot\omega) = g/(2\pi Cf)$. Here, I_R, I_C, G, C and ω are the current consuming energy, current flowing through dielectric capacitor (no energy consumption), leakage conductance, static capacitance and angular frequency of applied electric field, respectively. Hence, dielectric loss is falling smoothly with increasing frequency in this region. While polarization relaxation starts to dominate as increasing frequency. This behavior in relative high frequency region can be described by the Debye model [50]: $\varepsilon_r(\omega) = \varepsilon_\infty + (\varepsilon_s - \varepsilon_\infty)/(1+\omega^2\tau^2), \varepsilon_i(\omega) = (\varepsilon_s - \varepsilon_\infty)\omega\tau/(1+\omega^2\tau^2), \tan\delta = \varepsilon_i(\omega)/\varepsilon_r(\omega) = (\varepsilon_s - \varepsilon_\infty)\omega\tau/(\varepsilon_s + \varepsilon_\infty\omega^2\tau^2)$. Where $\varepsilon_r(\omega)$, $\varepsilon_i(\omega)$, ε_s, ε_∞ and τ are the real part of complex dielectric constant, imaginary part of complex dielectric constant, static or steady-state dielectric constant, high frequency dielectric constant, and relaxation time, respectively. The maximum value of tanδ is obtained when $\omega\cdot\tau = \sqrt{\varepsilon_s/\varepsilon_\infty}$ and the maximum value is $(\varepsilon_s - \varepsilon_\infty)/2\sqrt{\varepsilon_s\varepsilon_\infty}$. In addition, the fitted parameter values are listed in the table (Fig. 10(b)). Thus, there is a critical frequency in relative high frequency region.

4. Conclusion

Summarily, high-quality Mn-doped BNT (BNTM100*x*, $0 \leq x \leq 10\%$) films have been prepared by a modified sol-gel method. At room temperature, crystalline structure undergoes local lattice distortions instead of phase transitions with increasing Mn composition. The temperature-dependent Raman and SE spectra reveal an intermediate phase between the ferroelectric rhombohedral and paraelectric tetragonal phases, and the phase diagram of Mn-doped BNT films has been proposed. The direct optical band gap is about 3.96 eV, which originates from electron transformation from O-2*p* to Ti-3d/Bi-6*p* states at the Γ-point. Moreover, Mn-dopant enhances ferroelectric ($P_r \sim 32.1\ \mu C/cm^2$) and energy storage properties ($W_{rec} \sim 19.84\ J/cm^3$), suppresses leakage current density by lengthening off-center displacement, decreasing pinning of domain wall and diminishing carriers concentration. The PFM results suggest that the 180° domain exists in films. The ohmic conduction mechanism and the FN is dominant current transport mechanism in low and high electric field regions, respectively. These results provide further information to develop BNT-based lead-free multifunctional devices.

Acknowledgments

One of the authors (W. Xu) is grateful to Y. Gao and Prof. X.J. Meng for technical supports. This work was financially supported by National Key Research and Development Program of China (Grant No. 2017YFA0303403), Natural Science Foundation of China (Grant Nos. 61674057, 61504156, and 61227902), Projects of Science and Technology Commission of Shanghai Municipality (Grant No. 15JC1401600), and the Program for Professor of Special Appointment (Eastern Scholar) at Shanghai Institutions of Higher Learning, the Fundamental Research Funds for the Central Universities, the Opening Project of Key Laboratory of Transparent Opto-functional Inorganic Materials, Chinese Academy of Sciences (No. KLTOIM201603), and the China and Germany Postdoctoral Exchange Program (No. 20161008).

References

[1] H.X. Fu, R.E. Cohen, Polarization rotation mechanism for ultrahigh electromechanical response in single-crystal piezoelectrics, Nature 403 (2000) 281–283.
[2] E. Cross, Lead-free at last, Nature 432 (2004) 24–25.
[3] A.S. Mischenko, Q. Zhang, J.F. Scott, R.W. Whatmore, N.D. Mathur, Giant electrocaloric effect in thin-film $PbZr_{0.95}Ti_{0.05}O_3$, Science 311 (2006) 1270–1271.
[4] C. Reitz, P.M. Leufke, H. Hahn, T. Brezesinski, Ordered mesoporous thin film ferroelectrics of biaxially textured lead zirconate titanate (PZT) by chemical solution deposition, Chem. Mater. 26 (2014) 2195–2202.
[5] T. Huang, S. Guo, L.P. Xu, C. Chen, H.S. Luo, J.H. Chu, Low temperature structural variations of $Na_{0.5}Bi_{0.5}TiO_3$-7%$BaTiO_3$ single crystal: evidences from optical ellipsometry and Raman scattering, J. Appl. Phys. 117 (2015), 224103.
[6] V.V. Shvartsman, D.C. Lupascu, Lead-free relaxor ferroelectrics, J. Am. Ceram. Soc. 95 (2012) 1–26.
[7] P. Li, W. Li, J.W. Zhai, B. Shen, H.R. Zeng, K.Y. Zhao, Composition dependence of phase structure and electrical properties of $BiMnO_3$-modified $Bi_{0.5}(Na_{0.8}K_{0.2})_{0.5}TiO_3$ thin films, RSC Adv. 5 (2015) 62713–62718.
[8] J.J. Zhu, J.Z. Zhang, K. Jiang, H.W. Zhang, Z.G. Hu, H.S. Luo, J.H. Chu, Coexistence of ferroelectric phases and phonon dynamics in relaxor ferroelectric $Na_{0.5}Bi_{0.5}TiO_3$ based single crystals, J. Am. Ceram. Soc. 99 (2016) 2408–2414.
[9] T. Huang, Z.G. Hu, G.S. Xu, X.L. Zhang, J.Z. Zhang, J.H. Chu, Inherent optical behavior and structural variation in $Na_{0.5}Bi_{0.5}TiO_3$-6%$BaTiO_3$ revealed by temperature dependent Raman scattering and ultraviolet-visible transmittance, Appl. Phys. Lett. 104 (2014), 111908.
[10] M. Tyagi, M. Kumari, R. Chatterjee, P. Sharma, Large magnetoelectric response in modified BNT based ternary piezoelectric [72.5($Bi_{1/2}Na_{1/2}TiO_3$)-22.5($Bi_{1/2}K_{1/2}TiO_3$)-5($BiMg_{1/2}Ti_{1/2}O_3$)]-magnetostrictive ($NiFe_2O_4$) particulate (0-3) composites, Appl. Phys. Lett. 106 (2015) 202904.
[11] M. Zeng, S.W. Or, H.L.W. Chan, First-principles study on the electronic and optical properties of $Na_{0.5}Bi_{0.5}TiO_3$ lead-free piezoelectric crystal, J. Appl. Phys. 107 (2010), 043513.
[12] B.N. Rao, A.N. Fitch, R. Ranjan, Ferroelectric-ferroelectric phase coexistence in $Na_{1/2}Bi_{1/2}TiO_3$, Phys. Rev. B 87 (2013), 060102(R).
[13] J.Y. Chen, Z.H. Tang, R.N. Tian, Y.L. Bai, S.F. Zhao, H. Zhang, Domain switching contribution to the ferroelectric, fatigue and piezoelectric properties of lead-free $Bi_{0.5}(Na_{0.85}K_{0.15})TiO_3$ films, RSC Adv. 6 (2016) 33834–33842.
[14] J.L. Yu, M. Zhang, M. Guo, Morphology evolution of lead-free ceramics: formation of $Bi_{0.5}Na_{0.5}TiO_3$ superstructures on a Ti substrate, CrystEngComm 13 (2011) 1953–1958.
[15] M.M. Hejazi, E. Taghaddos, A. Safari, Reduced leakage current and enhanced ferroelectric properties in Mn-doped $Bi_{0.5}Na_{0.5}TiO_3$-based thin films, J. Mater.

Sci. 48 (2013) 3511–3516.
[16] S. Zhang, M.J. Han, J.Z. Zhang, Y.W. Li, Z.G. Hu, J.H. Chu, Optoelectronic and ferroelectric properties of cerium-doped $(Na_{0.5}Bi_{0.5})(Ti_{0.99}Fe_{0.01})O_3$ nanocrystalline films on (111) $Pt/TiO_2/SiO_2/Si$: a composition-dependent study, ACS Appl. Mater. Interfaces 5 (2013) 3191–3198.
[17] M. Li, M.J. Pietrowski, R.A. De Souza, H. Zhang, I.M. Reaney, S.N. Cook, J.A. Kilner, D.C. Sinclair, A family of oxide ion conductors based on the ferroelectric perovskite $Na_{0.5}Bi_{0.5}TiO_3$, Nat. Mater. 13 (2014) 31–35.
[18] Q.L. Deng, J.Z. Zhang, T. Huang, L.P. Xu, K. Jiang, Y.W. Li, Z.G. Hu, J.H. Chu, Optoelectronic properties and polar nano-domain behavior of sol-gel derived $K_{0.5}Na_{0.5}Nb_{1-x}Mn_xO_{3-\delta}$ nanocrystalline films with enhanced ferroelectricity, J. Mater. Chem. C 3 (2015) 8225–8234.
[19] T. Kawae, Y. Terauchi, H. Tsuda, M. Kumeda, A. Morimoto, Improved leakage and ferroelectric properties of Mn and Ti codoped $BiFeO_3$ thin films, Appl. Phys. Lett. 94 (2009), 112904.
[20] M. Abazari, A. Safari, Effects of doping on ferroelectric properties and leakage current behavior of KNN-LT-LS thin films on $SrTiO_3$ substrate, J. Appl. Phys. 105 (2009), 094101.
[21] Y. Shuai, S.Q. Zhou, D. Bürger, H. Reuther, I. Skorupa, V. John, M. Helm, H. Schmidt, Decisive role of oxygen vacancy in ferroelectric versus ferromagnetic Mn-doped $BaTiO_3$ thin films, J. Appl. Phys. 109 (2011), 084105.
[22] Y.Y. Wu, X.H. Wang, C.F. Zhong, L.T. Li, Effect of anneal conditions on electrical properties of Mn-doped $(Na_{0.85}K_{0.15})_{0.5}Bi_{0.5}TiO_3$ thin films prepared by sol-gel method, J. Am. Ceram. Soc. 94 (2011) 1843–1849.
[23] H.B. Zhang, S.L. Jiang, K. Kajiyoshi, Pyroelectric and dielectric properties of Mn modified $0.82Bi_{0.5}Na_{0.5}TiO_3$-$0.18Bi_{0.5}K_{0.5}TiO_3$ lead-free thick films, J. Am. Ceram. Soc. 92 (2009) 2147–2150.
[24] D.Y. Wang, N.Y. Chan, S. Li, S.H. Choy, H.Y. Tian, H.L.W. Chan, Enhanced ferroelectric and piezoelectric properties in doped lead-free $(Bi_{0.5}Na_{0.5})_{0.94}$-$Ba_{0.06}TiO_3$ thin films, Appl. Phys. Lett. 97 (2010), 212901.
[25] W. Li, H.R. Zeng, J.G. Hao, J.W. Zhai, Enhanced dielectric and piezoelectric properties of Mn doped $(Bi_{0.5}Na_{0.5})TiO_3$-$(Bi_{0.5}K_{0.5})TiO_3$-$SrTiO_3$ thin films, J. Alloys Compd. 580 (2013) 157–161.
[26] W.W. Ge, H. Liu, X.Y. Zhao, W.Z. Zhong, X.M. Pan, T.H. He, D. Lin, H.Q. Xu, X.P. Jiang, H.S. Luo, Growth, optical and electrical properties of pure and Mn-doped $Na_{0.5}Bi_{0.5}TiO_3$ lead-free piezoelectric crystals, J. Alloys Compd. 462 (2008) 256–261.
[27] Y.-N. Xu, W.Y. Ching, Electronic structure of $(Na_{1/2}Bi_{1/2})TiO_3$ and its solid solution with $BaTiO_3$, Phil. Mag. Lett. 80 (2000) 1141–1151.
[28] D.K. Khatua, T. Mehrotra, A. Mishra, B. Majumdar, A. Senyshyn, R. Ranjan, Anomalous influence of grain size on the global structure, ferroelectric and piezoelectric response of $Na_{0.5}Bi_{0.5}TiO_3$, Acta Mater. 134 (2017) 177–187.
[29] M.K. Niranjan, T. Karthik, S. Asthana, J. Pan, U.V. Waghmare, Theoretical and experimental investigation of Raman modes, ferroelectric and dielectric properties of relaxor $Na_{0.5}Bi_{0.5}TiO_3$, J. Appl. Phys. 113 (2013), 194106.
[30] H.F. Lü, S.Y. Wang, X.S. Wang, The electronic properties and lattice dynamics of $(Na_{0.5}Bi_{0.5})TiO_3$: from cubic to tetragonal and rhombohedral phases, J. Appl. Phys. 115 (2014), 124107.
[31] T. Huang, P. Zhang, L.P. Xu, C. Chen, J.Z. Zhang, Z.G. Hu, H.S. Luo, J.H. Chu, Electronic structures and abnormal phonon behaviors of cobalt-modified $Na_{0.5}Bi_{0.5}TiO_3$-6%$BaTiO_3$ single crystals, AIP Adv. 6 (2016), 105311.
[32] C.Q. Li, Q.R. Yao, J.Z. Zhang, Z.G. Hu, F.F. Wang, A.Y. Liu, W.Z. Shi, J.H. Chu, Dramatic influence of Dy^{3+} doping on strain and domain structure in lead-free piezoelectric $0.935(Na_{1/2}Bi_{1/2})TiO_3$-$0.065BaTiO_3$ ceramics, AIP Adv. 5 (2015), 127118.
[33] J.Z. Zhang, Z.H. Duan, H. Zhang, M.J. Han, Y.W. Li, Z.G. Hu, J.H. Chu, Improved electric behaviors of the $Pt/Bi_{1-x}La_xFe_{0.92}Mn_{0.08}O_3/n^+$-Si heterostructure for nonvolatile ferroelectric random-access memory, J. Mater. Chem. C 1 (2013) 6252–6258.
[34] S.P. Pavunny, A. Kumar, R.S. Katiyar, Raman spectroscopy and field emission characterization of delafossite $CuFeO_2$, J. Appl. Phys. 107 (2010), 013522.
[35] J.Z. Zhang, X.G. Chen, Y.D. Shen, Y.W. Li, Z.G. Hu, J.H. Chu, Synthesis, surface morphology, and photoluminescence properties of anatase iron-doped titanium dioxide nano-crystalline films, Phys. Chem. Chem. Phys. 13 (2011) 13096–13105.
[36] S. Adachi, Model dielectric constants of GaP, GaAs, GaSb, InP, InAs, and InSb, Phys. Rev. B 35 (1987) 7454–7463.
[37] V. Dorcet, G. Trolliard, P. Boullay, Reinvestigation of phase transitions in $Na_{0.5}Bi_{0.5}TiO_3$ by TEM. Part I: first order rhombohedral to orthorhombic phase transition, Chem. Mater. 20 (2008) 5061–5073.
[38] G. Trolliard, V. Dorcet, Reinvestigation of phase transitions in $Na_{0.5}Bi_{0.5}TiO_3$ by TEM. Part II: second order orthorhombic to tetragonal phase transition, Chem. Mater. 20 (2008) 5074–5082.
[39] P. Li, W. Li, S.H. Liu, Y. Zhang, J.W. Zhuai, H. Chen, Reduced leakage current, enhanced ferroelectric and dielectric properties of (La, Fe)-codoped $Bi_{0.5}Na_{0.5}TiO_3$-based thin films, Ceram. Int. 41 (2015) S344–S348.
[40] C.H. Yang, G.D. Hu, W.B. Wu, H.T. Wu, F. Yang, Z.Y. Lu, L. Wang, Reduced leakage current, enhanced ferroelectric and dielectric properties in (Ce,Fe)-codoped $Na_{0.5}Bi_{0.5}TiO_3$ film, Appl. Phys. Lett. 100 (2012), 022909.
[41] C.C. Jin, F.F. Wang, C.M. Leung, Q.R. Yao, Y.X. Tang, T. Wang, W.Z. Shi, Enhanced ferroelectric and piezoelectric response in Mn-doped $Bi_{0.5}Na_{0.5}$-TiO_3-$BaTiO_3$ lead-free film by pulsed laser deposition, Appl. Surf. Sci. 283 (2013) 348–351.
[42] Z.H. Zhou, J.M. Xue, W.Z. Li, J. Wang, H. Zhu, J.M. Miao, Ferroelectric and electrical behavior of $(Na_{0.5}Bi_{0.5})TiO_3$ thin films, Appl. Phys. Lett. 85 (2004) 804–806.
[43] Z.T. Yang, H.L. Du, S.B. Qu, Y.D. Hou, H. Ma, J.F. Wang, J. Wang, X.Y. Wei, Z. Xu, Significantly enhanced recoverable energy storage density in potassium-sodium niobate-based lead free ceramics, J. Mater. Chem. A 4 (2016) 13778–13785.
[44] X.H. Hao, A review on the dielectric materials for high energy-storage application, J. Adv. Dielect. 3 (2013), 1330001.
[45] G. Viola, H. Ning, M.J. Reece, R. Wilson, T.M. Correia, P. Weaver, M.G. Cain, H. Yan, Reversibility in electric field-induced transitions and energy storage properties of bismuth-based perovskite ceramics, J. Phys. D Appl. Phys. 45 (2012), 355302.
[46] L.H. Luo, B.Y. Wang, X.X. Jiang, W.P. Li, Energy storage properties of (1-x)$(Bi_{0.5}Na_{0.5})TiO_3$-x$KNbO_3$ lead-free ceramics, J. Mater. Sci. 49 (2014) 1659–1665.
[47] J.G. Wu, J. Wang, D.Q. Xiao, J.G. Zhu, Leakage mechanism of cation-modified $BiFeO_3$ thin film, AIP Adv. 1 (2011), 022138.
[48] J.G. Wu, J. Wang, D.Q. Xiao, J.G. Zhu, Multiferroic and fatigue behavior of silicon-based bismuth ferrite sandwiched structure, J. Mater. Chem. 21 (2011) 7308–7313.
[49] B.K. Vashisth, J.S. Bangruwa, A. Beniwal, S.P. Gairola, A. Kumar, N. Singh, V. Verma, Modified ferroelectric/magnetic and leakage current density properties of Co and Sm co-doped bismuth ferrites, J. Alloys Compd. 698 (2017) 699–705.
[50] Y.W. Li, Z.G. Hu, F.Y. Yue, G.Y. Yang, W.Z. Shi, X.J. Meng, J.L. Sun, J.H. Chu, Properties of highly (100) oriented $Pb(Mg_{1/3},Nb_{2/3})O_3$-$PbTiO_3$ films on $LaNiO_3$ bottom electrodes, Appl. Phys. Lett. 91 (2007), 232912.